RESEARCH ARTICLE

ADVANCED FUNCTIONAL MATERIALS
www.afm-journal.de

MXene-Triggered 3D Printing of Gradient-Modulus Iontronic Pressure Sensors for Adaptive Robotic Grasping

*Yuanjie Jiang, Chendong Zhao, Zhuoyu Song, Rui Jia, Jimei Liu, Xinyu Liu, Qinglong He, Wenchao Gao, Caofeng Pan, Valeria Nicolosi, and Chuanfang Zhang**

Flexible capacitive pressure sensors are critical components in emerging applications such as electronic skin, human-machine interfaces, and soft robotics. However, achieving a balance between high sensitivity and a wide linear range remains a key challenge. Here, a synergistic strategy is reported that integrates printable gradient-modulus hydrogels with microstructured architectures to mitigate this performance trade-off. It is revealed that MXene plays a critical role in fine-tuning the elastic moduli of the hydrogel inks via the so-called MXene triggering chemistry, the latter greatly boosts the radical generation for rapid polymerization kinetics. This enables the minutes-scale printing of vertically modulus-graded (stiff-medium-soft layers from top to bottom) microdome structures. Such a rational design effectively delays the structural densification and achieves progressive, layer-by-layer deformation under pressure, leading to a high sensitivity of 538 kPa^{-1} across a broad pressure range (up to 440 kPa). The great potential of the rapid-printed pressure sensing arrays in recognizing object stiffness is further demonstrated, and provides real-time spatial capacitance feedback during grasping tasks by integrating into a robotic gripper. This work offers a scalable and programmable strategy for innovating material modulus and structural geometry, opening new pathways toward high-performance tactile sensors for intelligent sensing and adaptive robotics.

1. Introduction

With the continuous advancement of flexible electronics and human-machine interface technologies, the demand on flexible pressure sensors has surged in applications ranging from electronic skin and health monitoring to wearable robotics and artificial intelligence.[1–4] As functional demands grow increasingly complex, the requirements on sensitivity, linearity, and durability have become more stringent.

Among various sensing mechanisms, capacitive pressure sensors have attracted substantial attention due to their structural simplicity, fast response, low power consumption, and excellent repeatability.[5–8] However, achieving simultaneous high sensitivity and a wide linear sensing range remains an enduring challenge. To date, performance enhancement has primarily relied on engineering the dielectric layer with compressible microstructures such as pyramids, domes, or interlocking pillars.[9–14] While these architectures enhance deformability and capacitance variation under low pressure, they typically suffer from structural hardening and stiffness saturation under high loads, resulting in nonlinear responses and early signal plateauing (Figure S1a, Supporting Information). This limits the effective sensing range and complicates subsequent signal processing.

To mitigate these limitations, recent studies have introduced structural gradient designs that modulate microstructure dimensions – such as height, pitch, or aspect ratio – to achieve delayed structural collapse and broaden the linear response regime. Hierarchical interlocked architectures and biomimetic gradient arrays demonstrate stepwise deformation pathways, allowing the sensor to maintain signal responsiveness over extended pressure intervals. These strategies induce a nonlinear stiffness gradient, enabling progressive stress transfer and subsequent

---

Y. Jiang, C. Zhao, R. Jia, J. Liu, X. Liu, Q. He, C. Zhang
College of Materials Science & Engineering
Sichuan University
Chengdu, Sichuan 610065, P.R. China
E-mail: chuanfang.zhang@scu.edu.cn

Z. Song
Department of Engineering Mechanics
Dalian University of Technology
Dalian, Liaoning 116024, P. R. China

W. Gao
Beijing Institute of Nanoenergy and Nanosystems
Chinese Academy of Sciences
Beijing 101400, P. R. China

C. Pan
Institute of Atomic Manufacturing
International Research Institute for Multidisciplinary Science
Beihang University
Beijing 100191, P. R. China

V. Nicolosi
School of Chemistry
Centre for Research on Adaptive Nanostructures and Nanodevices (CRANN) & Advanced Materials and BioEngineering Research (AMBER)
Trinity College Dublin
Dublin 2, Dublin D02 PN40, Ireland

The ORCID identification number(s) for the author(s) of this article can be found under https://doi.org/10.1002/adfm.202522891

DOI: 10.1002/adfm.202522891

deformation. In particular, recent works have demonstrated iontronic or capacitive sensors employing graded micro-domes or hierarchical interlocks with high sensitivity and nearly ideal linearity ($R^2 > 0.995$) across wide pressure ranges, confirming the effectiveness of gradient designs in overcoming geometric saturation effects.[15–17] However, fabrication still often relies on complex micro-molding or pattern-transfer processes with limited scalability and poor interlayer adhesion, hindering device uniformity and reliability.[5,18–19]

On the other hand, material-based strategies, particularly modulus gradients via multilayered casting, ionic diffusion, or infiltration techniques, have shown promise in extending the pressure linear range.[20–22] However, these methods often face limited design freedom, weak interfacial bonding, and poor reproducibility. In other words, such strategies often improve linearity at the cost of sensitivity, leaving the "trade-off dilemma" unresolved (Figure S1b, Supporting Information).

3D printing offers inherent programmability in both structural geometry and material composition, enabling the free-design of hierarchical architectures and spatially graded mechanical properties within a single fabrication platform.[23–24] Recent demonstrations have validated its capabilities to construct functionally graded layers and complex multi-material integrations, providing a pathway toward device-level performance optimization and manufacturing scalability.[25–27] However, translating conventional sensing materials into stable gradient architectures via 3D printing remains challenging, since most elastomers or hydrogels lack the rapid gelation or solidification behavior needed to preserve delicate features, leading to structural collapse or interlayer mismatch. These shortcomings are particularly detrimental for gradient designs, where precise modulus distribution and geometric fidelity are essential to achieving staged deformation and sustained linearity. Therefore, the development of printable materials capable of spatially programmable gelation – while maintaining tunable mechanical properties – is essential to fully unlocking the structural design freedom of additive manufacturing.

Recently, 2D transition metal carbides and nitrides (MXenes) have attracted considerable attention for soft electronics due to their high electrical conductivity, abundant surface terminations (−OH, −O, −F), and transition-metal active sites, which can modulate radical polymerization and accelerate network formation.[28] These chemical features enable rapid, composition-dependent gelation of hydrogel matrices, providing a critical pathway to construct stable, mechanically graded microstructures directly via 3D printing – an approach that, to the best of our knowledge, has not yet been reported.

To this end, we report a synergistic strategy integrating programmable hydrogel chemistry with 3D-printed microstructures to realize capacitive pressure sensors combining high sensitivity and extended linearity. We formulate MXene-poly(vinyl alcohol) (PVA)/ polyacrylic acid (PAA) hydrogel inks whose modulus can be precisely tuned through the unique MXene triggering effect, the latter greatly boosts the radical generation for rapid polymerization kinetics. With direct ink writing (DIW) of spatially modulus-graded, dome-shaped architectures, we achieve delayed saturation and enhanced linearity (**Figure 1a,b**). Compared to uniform structures, our gradient design provides superior strain buffering and stress redistribution, yielding high sensitivity (538.47 kPa^{-1}), a wide linear range (up to 440 kPa), stable cycling (>1500 cycles), and consistent response across multiple channels. We further demonstrate the potential application of a 3D printed microstructure-based robotic gripper in sensitively grasping different objects with spatially resolved force feedback. This work presents a generalizable framework for the co-innovating of material stiffness and structure-induced mechanical response via additive manufacturing, offering new avenues for high-performance tactile sensors in intelligent robotics, soft electronics, and biomedical diagnostics.

2. Results and Discussion

2.1. MXene-Regulated Radical Polymerization and Hydrogel Ink Modulation

In this work, we employ $Ti_3C_2T_x$ MXene (denoted as MXene if not specifically mentioned) to accelerate the radical polymerization kinetics as well as to tailor the hydrogel ink modulus. To this end, MXene was prepared using the wet-chemistry route. As shown in Figure S2 (Supporting Information), after etching the Ti_3AlC_2 MAX precursor, a multilayered MXene with accordion-like morphology is achieved. Further upon delamination, few-layered, smooth MXene flakes with a size of ≈8 µm are achieved (Figure S3, Supporting Information). The X-ray diffraction pattern indicates that the freestanding MXene film (by filtrating the MXene colloidal solution) only exhibits peaks corresponding to (00*l*) planes, suggesting the ordered stacking of MXene nanosheets and confirming the successful MXene synthesis (Figure S4, Supporting Information). The optical image validates the homogeneous MXene dispersion with a typical metallic luster and good colloidal stability (**Figure 2a**). Transmission electron microscopy (TEM, Figure 2b) confirms the ultrathin 2D sheet structure of delaminated MXene flakes with a lateral size of ≈8 µm. These MXene flakes are of ≈1.2 nm in thickness, confirmed by the atomic force microscopy (AFM, Figure 2c).

Electron paramagnetic resonance (EPR) spectroscopy was employed to verify the critical role of MXene in the free radical polymerization (Figure 2d). The reference solution containing ammonium persulfate (APS) only exhibits negligible OH· radical signals. In contrast, upon addition of trace MXene, the solution shows pronounced signals corresponding to DMPO-OH· and DMPO-$SO_4\cdot^-$, respectively. This clearly indicates that MXene accelerates APS decomposition to generate reactive radicals such as ·OH and $SO_4\cdot^-$, enabling rapid initiation of the polymerization process. This phenomenon is supported by recent studies demonstrating that MXene lowers the dissociation enthalpy of persulfate compounds, serving as a solid-phase radical promoter.[28–29] Such an effect is crucial for rapid solidification during layer-by-layer printing. Furthermore, this mechanism lays the molecular foundation for the macroscopic changes in gelation rate and hydrogel modulus with increasing MXene concentration, as discussed below. This catalytic effect is not universal among nanofillers. Beyond serving as a radical initiator, MXene offers distinct advantages compared with other nanomaterials occasionally reported to accelerate persulfate decomposition: its rich surface terminations (−OH, −O, −F) and transition-metal sites act as highly efficient catalytic centers, as well as the high conductivity of MXene facilitates electron transfer. These

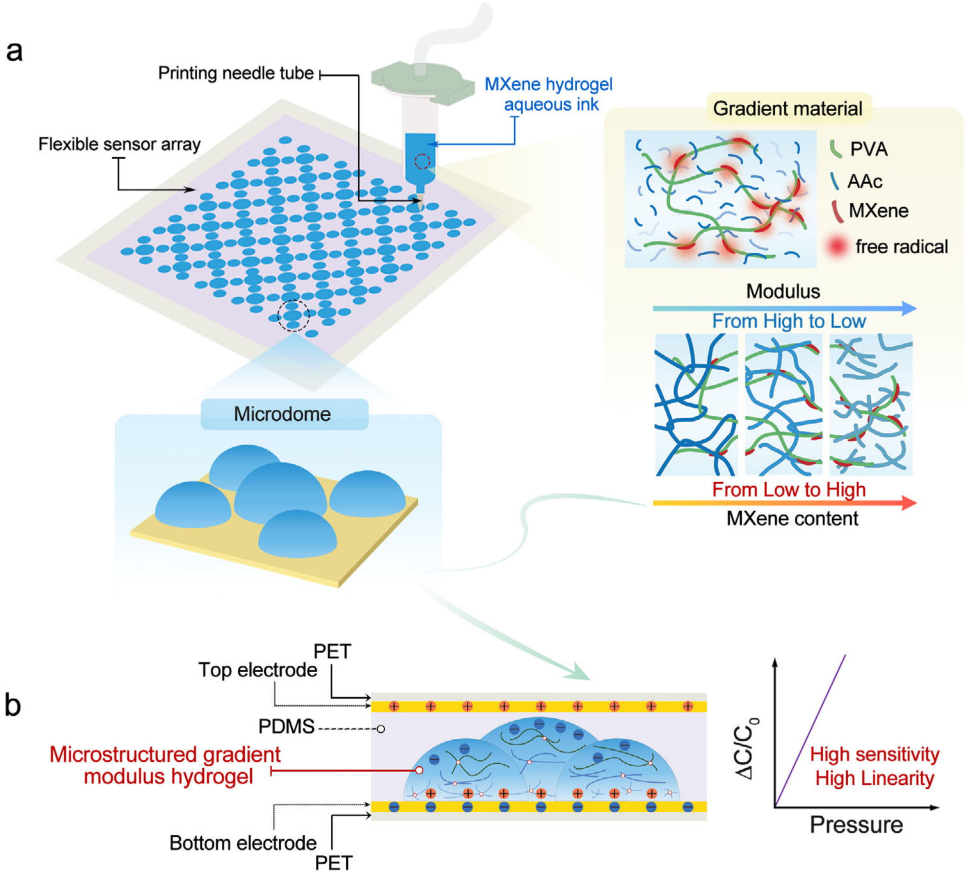

Figure 1. Schematic illustration of the design strategy for high-performance flexible pressure sensors based on microstructured gradient modulus hydrogels. a) The scheme of 3D printing of a flexible sensor array using MXene-hydrogel aqueous inks. Each microdome is composed of a spatially programmed gradient modulus, achieved by varying MXene content from top to bottom. The gradient structure is achieved by sequentially printing hydrogel inks with different MXene concentrations and immediately crosslinking with APS, enabling continuous modulation of mechanical stiffness (from high to low modulus). b) The printed microstructured hydrogel is integrated between the top and bottom PET/Cu electrodes to form an iontronic pressure sensor. Under external loading, the integrated gradient-modulus and architecture design induce a cascade deformation pathway, thereby achieving high sensitivity together with an extended linear response.

features, together with its excellent colloidal stability in aqueous systems, enable uniform and controllable hydrogel gelation, distinguishing MXene as a particularly suitable choice for constructing printable iontronic hydrogels.[30–32]

Real-time infrared (IR) thermal imaging was conducted to visualize the accelerated polymerization kinetics of MXene-PVA/PAA inks (ink formulation can be found in Figure S5, Supporting Information). As shown in Figure 2e, the pristine hydrogel (0% MXene) shows negligible thermal activity over extended periods, in sharp contrast to the clear thermal response once introducing MXene. This suggests that MXene has greatly accelerated the radical polymerization kinetics at room temperature. The thermal imaging also reveals that the MXene content largely controls the heating rate, indicative of the polymerization speed is MXene content-dependent (Figures S6–S8, Supporting Information). In line with our previous explanation, MXene facilitates the decomposition of APS into $SO_4{\cdot}^-$ and ·OH radicals through surface redox reactions, thereby accelerating radical generation and triggering faster network formation.[28]

Fourier-transform infrared (FT-IR) spectroscopy was employed to elucidate how MXene alters the chemical interactions within the hydrogel matrix. The broad -OH stretching band (peak centered near ≈3300 cm^{-1}) can be attributed to the hydrogen bonding among PVA, PAA, and absorbed water. After adding MXene, the intensity of the —COOH stretching vibration band (≈1700 cm^{-1}, due to the protonated carboxylic acid groups on PAA) progressively decreases. The overall weakening of -OH and -COOH peaks, accompanied by a subtle redshift, reflects reduced hydrogen-bond network density and decreased hydrogen bond interactions.[33–36] The relatively stable -CH_2 bending vibration (≈1420 cm^{-1}) indicates that the PVA skeleton is largely retained. In other words, MXene incorporation affects supramolecular interactions rather than disrupts the covalent bonds. This is further confirmed by the X-ray photoelectron spectroscopy (XPS), as the redshift (≈0.2 eV) of peaks corresponding to C—C and C—O bonds is observed on the high-resolution C1s spectrum in the MXene-PVA/PAA hydrogel sample (Figure 2g). This suggests that MXene participates in interfacial coupling and alters its local bonding environment through assisting the local electronic redistribution.

We further reveal how MXene incorporation alters the mesoscale network topology and, thereafter hydrogel's modulus.

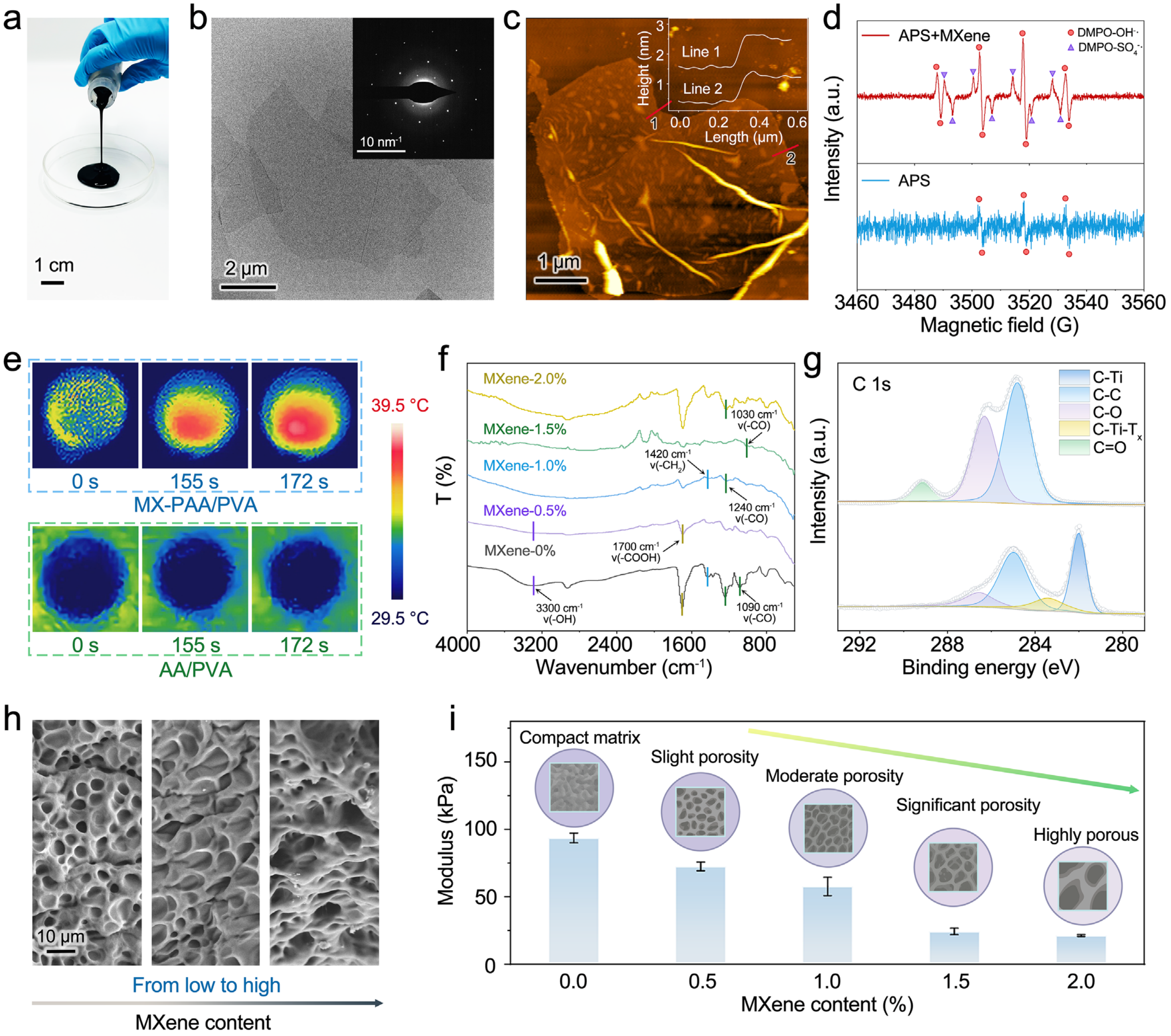

Figure 2. Characterizations of MXene inks and hydrogels. a) Optical image of delaminated MXene ink, showing metallic luster and excellent colloidal stability. b) TEM image confirming the ultrathin 2D sheet morphology of delaminated MXene flakes. c) AFM height profile revealing single- and few-layer structures of MXene nanosheets. d) EPR evidence for MXene-triggered radical generation. e) Thermal imaging of MXene-regulated gelation kinetics. f) FT-IR spectroscopy of hydrogel samples with different MXene contents. g) XPS of C1s spectrum in hydrogel without (up) and with (bottom) MXene. h) SEM images of freeze-dried hydrogels (0.5%, 1.0%, 1.5% MXene), showing increasing pore size with MXene content. i) Compressive modulus of hydrogels containing 0%-2.0% MXene, revealing a steady decrease due to MXene alters the topological network (shown in the insets).

Scanning electron microscopy (SEM) images of lyophilized hydrogels clearly indicate the evolution from small, discrete cavities to more open, interconnected porous networks as increasing MXene content (Figure 2h; Figures S9–S13, Supporting Information). This validates MXene's dual role: while it accelerates free radical generation, it simultaneously interferes with polymer chain entanglement and long-range network propagation. The looser, less crosslinked networks with enlarged pores dramatically decrease the hydrogel's compressive modulus from ≈94 kPa (0% MXene) to ≈21 kPa (2.0% MXene) (Figure 2i). Such counterintuitive softening agrees with recent reports that excessive 2D nanofillers can disrupt polymer continuity and weaken mechanical integrity, rather than reinforcing it, due to spatially inhomogeneous crosslinking and defect-rich network formation.[30,37–38] In addition to modulus regulation, MXene incorporation also influences the hydrogel's electromechanical response and cyclic stability, as evidenced by strain-dependent resistance variation (Figure S14, Supporting Information) and reproducible loading-unloading behavior over successive cycles (Figure S15, Supporting Information). As such, hydrogel inks with 0.5%–1.5% MXene are formulated with an optimal modulus range (20 ≈ 70 kPa) for subsequent 3D printing of modulus-gradient pressure sensors.

2.2. Simulation-Guided Geometric and Material Hybridization Enables Balanced Sensitivity and Linearity

Next, we perform finite element simulations (ABAQUS/Standard) to determine the geometry of the sensors such that the sensitivity and pressure range are well decoupled in the 3D printed architectures. We choose hemispherical dome-based architectures instead of pyramidal structures or pillars due to they former provide excellent deformability, ensuring a broad linear range while retaining reasonable sensitivity.[39] Several hydrogel geometries with distinct modulus configurations are first simulated, including homogeneous low (PL), medium (PM), and high (PH), as well as two gradient-modulus designs: GLMH, where modulus increases from top to bottom (low-medium-high), and GHML, where modulus decreases from top to bottom (high-medium-low) (**Figure** 3a; schematic in Figure S16, Supporting Information). Clearly, before normalizing by the initial contact area, PL structure exhibits the highest sensitivity in the low-pressure regime, while PH demonstrates an extended linear region (Figure S17, Supporting Information) with much lower sensitivity.

In the gradient-modulus sample, the GLMH structure exhibits a high deformation rate under small loads due to the top soft layer; however, it encounters early mechanical saturation (as a result of the concentrated internal stress). On the other hand, GHML showcases a modest initial sensitivity but an extended quasi-linear regime, which is reasonably attributed to the gradual pass of the applied stress to the underlying softer layers, allowing the well to maintain of high responsiveness over a broader pressure range such that early saturation is avoided.[40–42] As a result, GHML achieves the highest overall $\Delta A/A_0$ in the full loading window (Figure 3b), demonstrating the best trade-off between sensitivity and linearity – an essential criterion for practical pressure sensors. These findings offer quantitative support for the design of gradient-modulus architectures toward next-generation high-performance pressure sensors.

Considering the influence of dome packing density on pressure responsiveness, we designed three types of micro-dome layouts with varying surface coverage (Figure 3c). Clearly, the 4-microdome layout showcases the highest sensitivity (due to its larger inter-dome spacing allowing for more unconstrained deformation) but quickly gets saturated, indicative of limited linear range. On the other hand, the 9-microdome layout exhibits a moderate sensitivity and pressure span, likely due to the crowd pattern that restricts further deformation upon compression and is consistent with previously reported mechanical coupling effects in dense microarrays.[19] However, the layout with a central dome surrounded by 4 corner ones demonstrates a high sensitivity with a linear range far beyond the 4-microdome array (Figure 3d). The well balance suggests the importance of moderate voids for structural deformation while preserving inter-dome mechanical integrity, thereby enhancing both responsiveness and linear pressure range. We further optimize the dome shape (e.g., the ratio of height to diameter) with identical gradient modulus distribution (Figure 3a,b) and dome arrangements (Figure 3c,d), revealing that the dome geometry with four ellipsoids surrounding a central hemisphere (4E1H) represents the best architecture (Figures S18–S20, Supporting Information). Unlike other designs, which either suffer from low sensitivity or early saturation, such a layout maintains a modest initial sensitivity while effectively extends the linear sensing range through the delayed participation of the central hemispherical dome. The finite-element simulations further confirm that the GHML-4E1H arrays exhibit favorable compressibility and uniform stress redistribution under applied pressure (Figure S21, Supporting Information). It should be noted that the GHML modulus gradient primarily broadens the high-pressure linearity by delaying structural saturation, while the 4E1H geometry enhances the low-pressure sensitivity. Their combination yields the observed synergistic optimization.

Based on the simulation results, we then formulate hydrogel inks and perform the 3D printing of pressure sensors with the desired dome geometry (4E1H) and modulus-gradient (GHML). By blending MXene dispersion with PVA/PAA and crosslinking agents, printable hydrogel inks with various MXene content (0.5%, 1% and 1.5%) are obtained (Figure 3e). All inks exhibit the shear-thinning behavior and high apparent viscosity, the prerequisites of smooth extrusion of filaments (Figure 3f; Figures S22–S27, Supporting Information). The representative 1.0% MXene ink behaves as a solid-like gel under low shear stress ($G' > G''$) and transits to a flowable liquid once the shear stress is beyond 420 Pa (Figure 3g). The excellent thixotropic recovery also suggests the rapid transition between solid-like and liquid-like states, allowing for the continuous extrusion upon applying the shear stress and rapid solidification once the external shear is removed (Figure 3h). Similar trends can also be observed in inks with 0.5% and 1.5% MXene, with increased MXene content corresponding to higher viscosity and higher critical stress before extruding the ink (Figures S22–S27, Supporting Information).

As such, patterns with desired dome geometry are directly printed using inks with varied MXene content. SEM images clearly indicate an ordered microdome array with consistent spacing and geometry coupled with an intended hybrid architecture as expected (Figure 3i). The dome heights and base radii are well preserved, indicating excellent printing accuracy and structural integrity (Figure S28, Supporting Information). The AFM tip-indentation model was further employed to check the spatial modulus gradient on the cross-section of a single dome. As demonstrated in Figure 3j, the top-down sections in the dome exhibit a gradually decreased modulus, in good agreement with the decreased MXene content along the bottom-up printing direction. This result validates that our MXene-modulated 3D printing strategy enables high-fidelity deposition of spatial modulus-gated hydrogel layers. These printed modulus-gated layers effectively withstand gradual deformation from 0% to 50% of applied stress without fracture or delamination, highlighting the robust interlayer adhesion and compatibility between the gradient layers (Figure 3k).

2.3. High-Sensitivity and Broad-Linearity Pressure Sensing Enabled by Printed Gradient-Modulus Microdomes

We then comprehensively evaluate the sensing performance of the 3D-printed iontronic pressure sensors. The assembling of the pressure sensor is schematically illustrated in Figure S29 (Supporting Information). Unlike conventional capacitive pressure sensors that predominantly rely on bulk geometric and

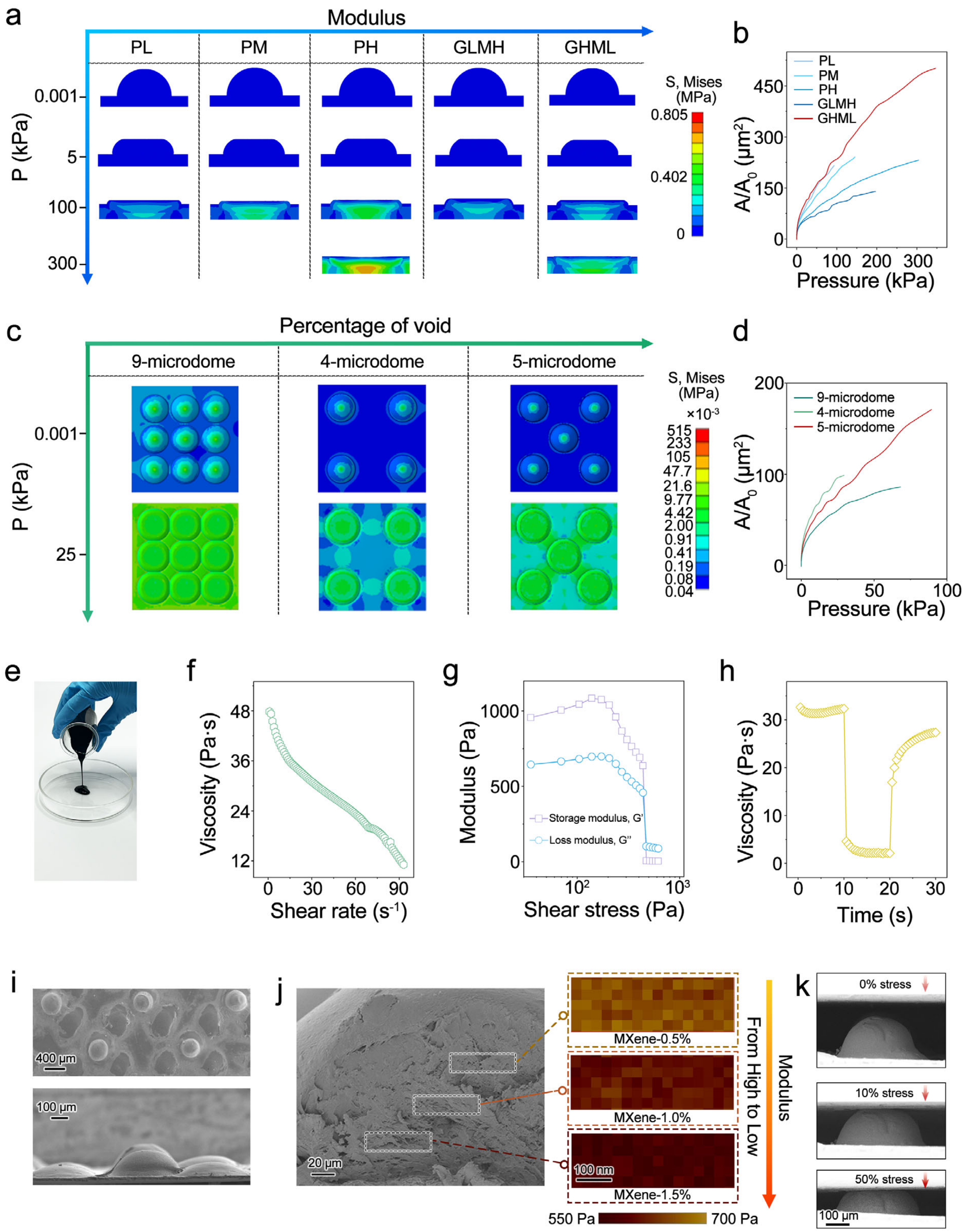

Figure 3. Finite element simulation-guided optimization of microstructure design and gradient modulus integration. a,b) Finite element analysis of hydrogel domes with varied modulus distributions (PL, PM, PH, GLMH, GHML), revealing their mechanical response and contact area evolution under increasing pressure. c,d) Effect of void fraction on pressure response: stress distribution and contact area of 9-, 4-, and 5-microdome arrays at different pressures. e) Photograph of printable MXene-based hydrogel ink. f–h) Rheological characterization of 1.0% MXene-based hydrogel ink: shear-thinning, yielding behavior, and recovery properties. i) Top-view and side-view SEM images of the 3D-printed microdome structure. j) Cross-sectional SEM and nanomechanical mapping confirming vertical modulus gradient. k) In situ SEM images showing dome deformation under progressive compressive loads.

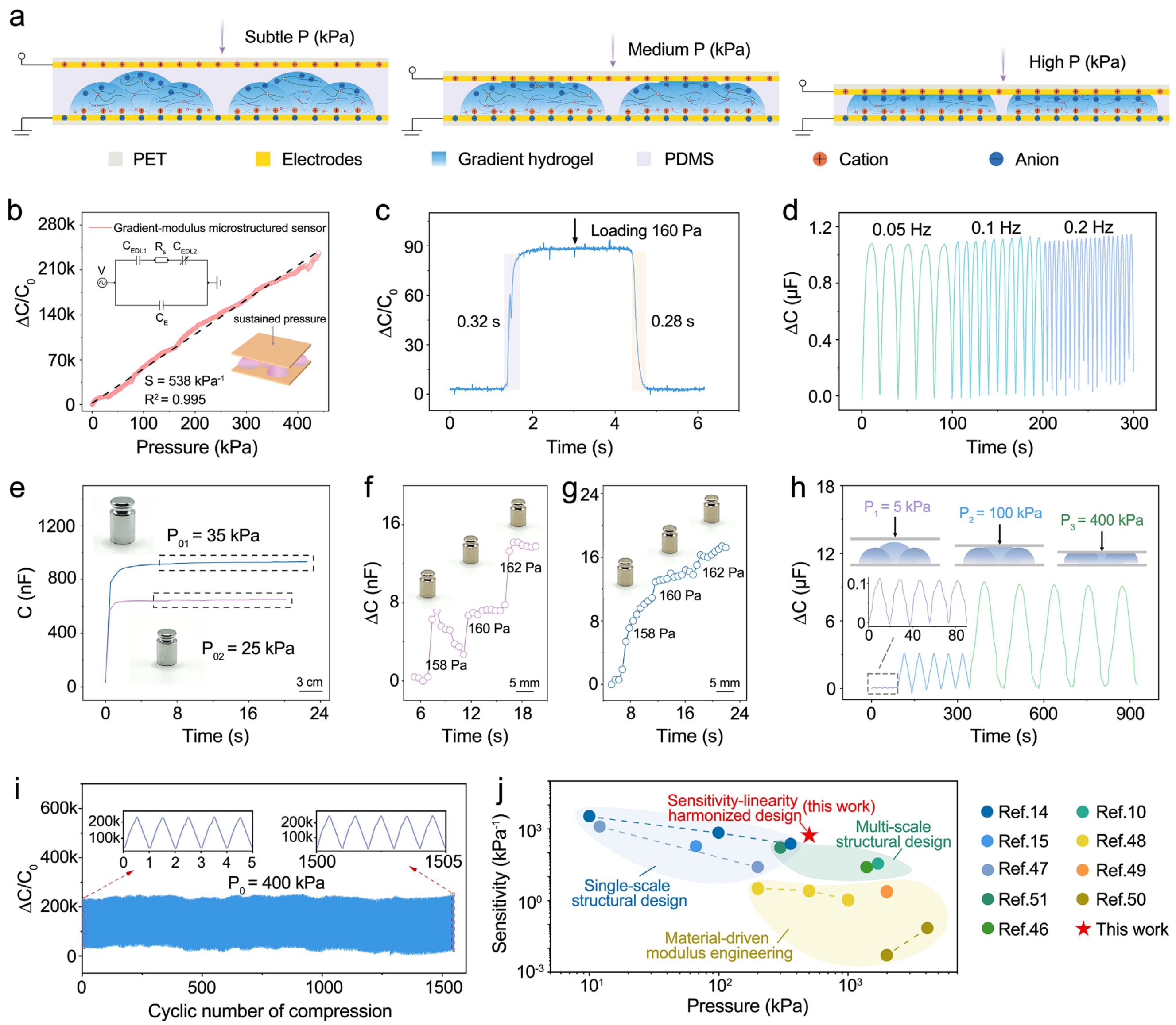

Figure 4. 3D-printed pressure sensor performance characterization. a) Schematic illustration of the capacitive sensing mechanism under subtle, medium, and high pressures, where both ion redistribution and effective contact area contribute to capacitance change, ensuring sensitivity across a broad range. b) Relative capacitance variation as a function of applied pressure, showing high sensitivity and linear response across a broad range. c) Dynamic response and recovery under small pressure. d) Frequency-dependent response of the sensor under triangular pressure inputs. e–g) Discrimination of minute pressure differences under different preload conditions. h) Capacitance response under gradually increasing loads. i) Long-term durability under continuous cycling at high pressure. j) Performance comparison with representative pressure sensors from literature, highlighting the optimal balance between sensitivity and linearity achieved by our iontronic pressure sensor design.

dielectric variations, our design further incorporates interfacial electrical double-layer (EDL) capacitance. This additional contribution maintains signal responsiveness under compression, thereby enabling pressure-adaptive sensitivity and an extended linear regime (**Figure** 4a).

As shown in Figure 4b, the sensor exhibits a nearly linear increase in $\Delta C/C_0$ across a broad pressure range up to ≈440 kPa, with a linearity coefficient of $R^2 = 0.995$ and an average sensitivity of ≈538 kPa^{-1}. The broad linear region originates from the synergistic effects of dynamic iontronic polarization and gradient mechanical modulation: the MXene-triggered hydrogel enhances the pressure-dependent interfacial C_{EDL}, while the gradient-modulus microdome redistributes stress and delays contact saturation.[10,30–31] Although finite element analysis (FEA) reveals nonlinear contact-area evolution, the measured capacitance-pressure curves appear highly linear because the electrical output reflects not only geometric deformation but also interfacial polarization, which amplifies incremental contact-area changes and effectively linearizes the electromechanical response.[10,43–44] These results demonstrate that the hierarchical structure and dynamic polarization coupling jointly yield high sensitivity and broad linearity – two attributes rarely achieved simultaneously in conventional capacitive sensors. The linearity coefficient ($R^2 = 0.995$) demonstrates the quantitative balance between sensitivity and range, comparable to or exceeding values reported in similar hydrogel-based capacitive sensors.[5,15]

The 3D-printed pressure sensors swiftly respond to external stimuli of 160 Pa with an apparent response/recovery time of ≈0.3 s (limited by the data sampling rate rather than the intrinsic device speed) (Figure 4c), and exhibit stable yet repeatable signal amplitudes without perceptible phase lag or attenuation under all testing frequencies (Figure 4d). The applied pressure in these frequency-dependent measurements followed a triangular waveform (0.05, 0.1, and 0.2 Hz), rather than a sinusoidal vibration, and the output capacitance accordingly shows a non-sinusoidal but phase-synchronized profile, faithfully tracking the cyclic mechanical input (Figure S30, Supporting Information). The consistent capacitance change within each cycle further affirms the sensor's excellent elasticity and rapid stress relaxation, rooted in the energy dissipation and recovery characteristics in the low-modulus bottom layer.

Moreover, the elaborated printed sensor is able to distinguish successive subtle increments based on preload conditions (Figure 4e). Impressively, the sensor gives consistent signal changes in response to ≈158 Pa at a preload of 25 kPa (Figure 4f) and 35 kPa (Figure 4g). The minor signal fluctuations observed in these low-pressure regimes mainly derive from instrumental noise, manual loading inconsistency, or ambient perturbations (e.g., table vibration, air turbulence), rather than from intrinsic sensor instability. Despite these unavoidable fluctuations, the minimum detection limit is as low as 22 Pa (Figure S31, Supporting Information), surpassing many other pressure sensors,[5,45] and can be well attributed to the unique architecture design by hybridizing the gradient modulus as well as dome arrangements. The central hemispherical dome provides gradual load diffusion, while the surrounding hemi-ellipsoidal domes enhance low-pressure sensitivity, enabling robust detection even within preloaded conditions, which mimics practical wearable or robotic scenarios.

To better understand the sensor's limit in detecting the compressive loads before saturation, we applied stepwise increasing pressure of 5, 100, and 400 kPa and collected the sensors′ capacitive response (Figure 4h). The sensor demonstrates rapid and consistent signal generation across the entire pressure range, maintaining clear and distinguishable $\Delta C/C_0$ plateaus at each loading step. Notably, the response magnitude increases proportionally with the applied load, confirming the broad dynamic range and excellent pressure resolution of the device.

Moreover, under a repeated loading-unloading regime at 400 kPa for over 1500 cycles, the printed sensor exhibits a highly stable $\Delta C/C_0$ signal without noticeable drift or fatigue-induced degradation (Figure 4i), indicative of excellent cycling performance. The cyclic stability is evaluated under cyclic loading (400 kPa) at ambient conditions (≈25 °C, 50 % RH), with a total duration of ≈5 h for 1500 cycles. Copper foil electrodes are used owing to their high conductivity and mechanical robustness; in this configuration, the copper surfaces are in contact with the solidified hydrogel rather than a free electrolyte, and no oxidation or signal drift is observed. Together, these results confirm the absence of mechanical hysteresis or signal fading, validating the sensor's long-term reliability for wearable and robotic applications.

We compare our device with representative pressure sensors reported in recent literature, mapping sensitivity versus effective pressure range (Figure 4j; Table S1, Supporting Information).[10,14–15,46–51] Single-scale microstructures achieve ultrahigh sensitivity but saturate within a narrow range, while multiscale or material-driven strategies extend range at the cost of responsiveness. In sharp contrast, our gradient-modulus microdome-structured pressure sensor realizes an optimal trade-off, combining high sensitivity with wide linearity. For further validation, control devices without microstructures, with single-scale domes, or with modulus gradients alone (Figures S32–S34, Supporting Information) all demonstrate either rapid saturation or low responsiveness, underscoring the advantage of synergistically integrating microgeometry with modulus gradients.

2.4. Application Demonstration: Real-Time Force Feedback in Robotic Grippers

Finally, to verify the functional applicability of our gradient-modulus pressure sensors in real-time intelligent tactile systems and for human-machine interactions, we integrate the 3D-printed pressure sensors into a soft robotic gripper equipped with three independently actuated fingers. As shown in **Figure 5a**, one sensor is affixed to each fingertip. The control system consists of an LCR meter for capacitance acquisition, real-time signal processing circuitry, and feedback-regulated actuation control (Figure 5b). The robotic gripper was employed to grasp objects with varying mechanical and geometric properties. The grasping process is divided into four sequential phases – prepare, grab, hold on, and put down – with corresponding real-time pressure feedback (ΔC) recorded independently by the three sensor channels (C1-C3). The excellent linearity ($R^2 = 0.995$) across a broad pressure range is also crucial for ensuring accurate and stable force feedback during robotic grasping. Owing to the nearly proportional pressure-capacitance relationship, the robotic controller can directly correlate $\Delta C/C_0$ changes with applied force, enabling adaptive modulation of gripping strength under different object stiffnesses without complex calibration or nonlinear correction. This capability underscores the practical advantage of the gradient-modulus design for achieving intelligent, reliable, and robust tactile sensing in soft robotics.

For the soft and geometrically irregular strawberry, the gripping process shows a relatively steep initial response slope, followed by a rapid stabilization (Figure 5c,f). Despite its asymmetric contour, the strawberry's moderate elasticity allows the sensors to establish stable contact, resulting in clear and synchronized ΔC signals. Real-time capacitive mapping confirms a balanced load distribution across the three fingers after contact adjustment. In contrast, the tofu square, despite being geometrically regular and cuboidal, demonstrates lower peak ΔC and larger inter-channel variation (Figure 5d,g). This can be attributed to two synergistic effects: (i) Its extremely soft and fragile internal structure introduces pronounced viscoelastic damping, which disperses contact stress and delays sensor stabilization, as reflected in the broader and more gradual ΔC curves; (ii) Its low structural stiffness makes it highly susceptible to local

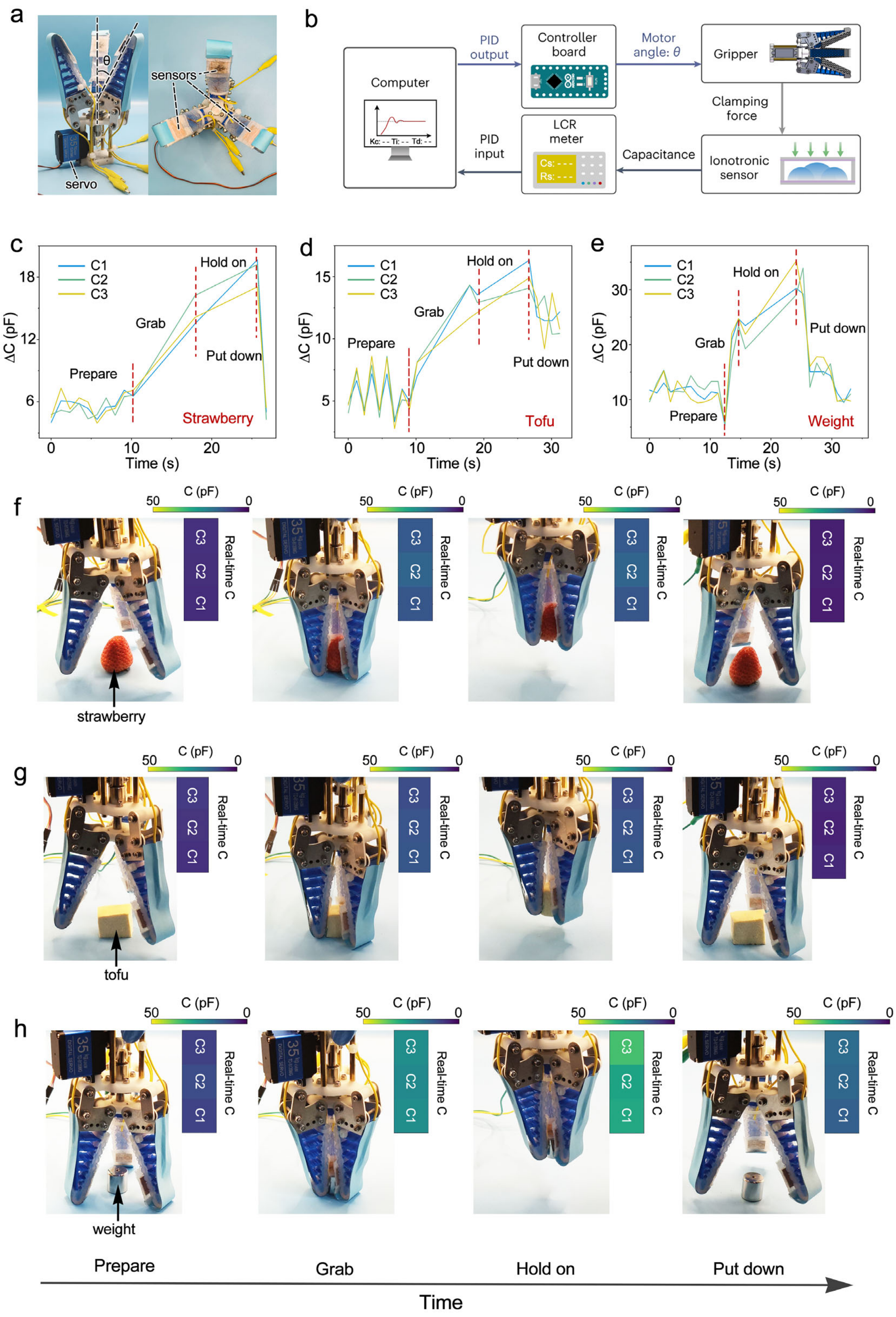

Figure 5. Robotic grasping demonstration using gradient-modulus microstructured capacitive sensors. a) Photograph of the robotic gripper integrated with 3D-printed gradient-modulus microstructured pressure sensors at each fingertip. b) Schematic of the closed-loop control system comprising the sensors, LCR meter, control unit, and computer. c–e) Real-time capacitance responses of the three-channel sensors during grasping of a strawberry, tofu, and a weight, respectively, with distinct stages of *Prepare, Grab, Hold on, Put down*, demonstrating accurate force discrimination and adaptive modulation. f–h) Reconstructed pseudo-color pressure maps during grasping of strawberry, tofu, and weight, showing spatially resolved pressure distribution and adaptive gripping stability. ("C" represents the relative change of capacitance with respect to the initial value).

indentation, which disturbs uniform pressure transmission across sensor contacts, resulting in more fluctuating and unbalanced signals during holding and release phases.

When grasping a rigid metal weight, the sensors exhibit the most symmetrical and stable responses (Figure 5e,h). Due to the cylindrical geometry and high modulus of the weight, force transmission is evenly distributed, the object subjects negligible deformation. Consequently, the ΔC values across C1-C3 rise synchronously and consistently, displaying minimal spatial shift during grasping.

In addition, we further validate adaptive force perception using cotton and table tennis balls (Figures S35 and S36, Supporting Information), with dynamic processes shown in Video S1 (Supporting Information). These comparative results illustrate that the sensor array can adaptively and independently sense pressure distributions during object manipulation, with signal dynamics jointly governed by the target's shape, mechanical stiffness, and viscoelastic damping behavior. More importantly, the high resolution and time-space fidelity of the electrical feedback establish the viability of this system for real-time tactile sensing in soft robotics. It demonstrates not only accurate pressure magnitude detection but also subtle perception of object properties and grasping dynamics. Collectively, the robotic gripper application validates the full sensing pipeline – from material-level gradient modulus to structural integration and multi-channel feedback – positioning our sensor as a promising platform for intelligent human-machine interfaces, wearable diagnostics, and compliant robotic manipulation.

3. Conclusion

In this work, we report on the decoupling of the sensitivity and wide linear response pressure range based on designing of gradient-modulus, elaborated microdome arrays. This is enabled by the unique MXene triggering chemistry, which greatly accelerates the free radical polymerization kinetics and allows the rapid 3D printing of modulus-gated dome architectures. Guided by the theoretical simulations, a vertically modulus-graded hybrid architecture with 4E1H dome arrangement is 3D printed, avoiding premature densification and expanding the usable deformation regime. As a result, the 3D-printed pressure sensor exhibits a broad linear detection range up to 440 kPa, a high sensitivity of 538 $\text{kPa}^{-1,}$ in addition to high durability over 1500 cycles. The excellent sensing performance ensures its precisely grasps objects when integrated in a robotic gripper. Our approach provides a scalable and programmable route for next-generation soft pressure sensors and opens up new opportunities for human-machine interactions, biomedical monitoring, and robotic manipulation, to name just a few.

4. Experimental Section

Materials: Titanium powder (Ti, 99.5%, 325 mesh), aluminum powder (Al, 99.5%, 325 mesh), graphite powder (Gr, 99%, 325 mesh), hydrochloric acid (HCl, Alfa, 37 wt.%), hydrofluoric acid (HF, Alfa, >40%), lithium chloride (LiCl, Alfa, 99%), ammonium persulfate (APS, Alfa, 98%, extra pure), acrylic acid (AAc, Alfa, 98%, extra pure), poly(vinyl alcohol) (PVA, Alfa, 87–89% hydrolyzed, high molecular weight), and N, N′-methylenebisacrylamide (MBAA, Alfa, 99%) were all purchased from AlFa and used as received unless otherwise specified. Polydimethylsiloxane (PDMS, Sylgard 184) was obtained from Dow Corning. Polyethylene terephthalate (PET) films (thickness: 50 µm) were purchased from Chengnuo Plastic Materials Co., Ltd. (Dongguan, China). Commercial high-purity oxygen-free copper sheets (thickness: 20 µm).

Synthesis of Ti_3AlC_2 MAX Phase: Ti, Al, and Gr powders were mixed in a molar ratio of 3: 2.2: 1.8 via manual grinding. The mixture was sintered at 1600 °C for 8 h under flowing argon to obtain Ti_3AlC_2 MAX blocks. The sintered products were crushed and sieved through a 400-mesh screen to yield MAX particles with sizes below 38 µm. To remove metallic impurities, the powders were etched in 9 M HCl for 18 h, followed by thorough washing with deionized water and vacuum drying at 80 °C for 6 h.

Synthesis and Delamination of $Ti_3C_2T_x$ MXene: $Ti_3C_2T_x$ MXene was synthesized by selective etching of the Al layer from MAX powder using a ternary acid mixture of HF: HCl: DI water (1: 6: 3 by volume) at 35 °C for 24 h. After etching, the product was centrifuged repeatedly and washed with deionized water until a neutral pH was reached.

To obtain delaminated MXene nanosheets, the multilayer sediment was dispersed in 0.5 M LiCl solution (50 mL per gram of MAX), stirred at 60 °C for 1 h under argon, and then centrifuged to remove unreacted materials. The supernatant containing few-layer MXene was collected and purified through multiple high-speed centrifugation cycles at 12 000 rpm to yield concentrated MXene ink.

Preparation of MXene-PVA/PAA Hydrogels: To prepare the hydrogel contrast sample, 2 g of PVA was dissolved in 18 g of deionized water at 90 °C with stirring for 2 h. The resulting solution was mixed with 1 g of AAc and 0.5 g of PVA stock solution. MBAA (30 mg) and APS (15 mg) were sequentially added as the crosslinker and initiator. The mixture was heated to 70 °C for an hour to complete gelation.

To fabricate MXene-composited hydrogels (MX-PVA/PAA), various concentrations of MXene ink (0.5, 1.0, and 1.5 wt.%) were incorporated into the above precursor solution. The mixture was homogenized and cured at room temperature for 10 min to form the MX-PVA/PAA hydrogel.

Fabrication of Gradient-Modulus Pressure Sensors: The sensor architecture consisted of six functional layers: bottom encapsulation, bottom electrode, spacer, sensing layer, top electrode, and top encapsulation. The sensing layer comprised a microdome array with vertical modulus gradients, fabricated via a layer-by-layer direct ink writing (DIW) method using a precision dispensing system (Shotmaster 300ΩX, Musashi Engineering).

MX-PVA/PAA inks (excluding APS) with decreasing MXene content (1.5, 1.0, and 0.5 wt.%) were sequentially printed from bottom to top. After each layer, a high-concentration APS mist (APS: DI water = 1: 4 by mass) was sprayed to induce localized gelation.

Copper foils were used as top and bottom electrodes. PDMS was cast at a 5: 1 base-to-curing agent ratio to form encapsulation and spacer layers, cured at 80 °C for 30 min.

Finite Element Analysis: Finite element simulations were performed in ABAQUS 2019/Standard to model the compression of 3D-printed hydrogel domes. Hydrogels were treated as nearly incompressible hyperelastic materials, with moduli extracted from MXene-PVA/PAA hydrogels (0.5%, 1.0%, 1.5% MXene corresponding to high, medium, and low stiffness, respectively) and fitted with the Yeoh model. Five-dome arrays (base diameter 500 µm) in quincunx layouts, including hemispheres and semi-ellipsoids (height/diameter = 0.6, 1.0), were simulated with rigid displacement loading, frictionless contact, and fixed substrates. Meshes employed C3D4H tetrahedral hybrid elements with local refinement; convergence was confirmed (<5% variation in contact area). Output parameters included equivalent pressure, contact area evolution, and normalized change $\Delta A/A_0$ (evaluated at 1 Pa preload) to evaluate effective sensing behavior.

Characterization and Measurements—Morphology and Structure: MXene morphology was characterized via SEM (Verios G4, Thermo Scientific), AFM (MFP-3D Origin+, Oxford), and TEM (Talos F200i). Crystalline phases were identified by XRD (Rigaku D/max 2550 V, Cu $K\alpha$, $\lambda = 1.5418$ Å).

Characterization and Measurements—Chemical Composition: FTIR spectroscopy (Nicolet IS50) and XPS (Thermo ESCALAB Xi$^+$) were used to probe bonding characteristics and elemental states.

Characterization and Measurements—Mechanical Testing: MXene hydrogels (MXene wt.% = 0%, 0.5%, 1.0%, 1.5%, 2.0%) moduli were measured using a universal testing machine (ZQ-990LB) under uniaxial compression. Microstructured gradient modulus hydrogel moduli were measured via AFM (Dimension Icon, Bruker).

Characterization and Measurements—Rheology: Viscosity and shear moduli were obtained via a rotational rheometer (Anton Paar, MCR302).

Characterization and Measurements—Electrical Response: Capacitance signals were recorded using a precision LCR meter (VC4090C, VICTOR).

Characterization and Measurements—Pressure Sensing Testing: The external pressure was applied and measured accurately by using a force gauge with a computer-controlled stage (ZQ-990LB, Zhiqu Precision Instrument Co., Ltd.).

Characterization and Measurements—Tactile Demonstration: Grasping experiments were performed using a pneumatic robotic gripper (FM-A4 V4/LS1[AS]-A8, Suzhou Soft-Touch Robotics, China) integrated with the fabricated sensors. Real-time electrical signals during object manipulation were recorded to validate force feedback behavior.

Supporting Information

Supporting Information is available from the Wiley Online Library or from the author.

Acknowledgements

Y.J.J., C.D.Z., and Z.Y.S. contributed equally to this work. The authors acknowledge the financial support from the National Natural Science Foundation of China (Grant No. 22479101, 00301054A1073, 22209118) and of Sichuan (Grant No. 2024NSFSC0233), the Fundamental Research Funds for the Central Universities (Nos. 1082204112A26, 20826044D3083, 20826041G4185, 20822041G4080) and Open research fund of State Key Laboratory of Mesoscience and Engineering (MESO-23-D06).

Conflict of Interest

The authors declare no conflict of interest.

Data Availability Statement

The data that support the findings of this study are available from the corresponding author upon reasonable request.;

Keywords

3D printing, adaptive robotic grasping, hydrogels, iontronic pressure sensors, MXene

Received: August 29, 2025
Revised: October 10, 2025
Published online: November 10, 2025

---

[1] S. Sundaram, P. Kellnhofer, Y. Li, J.-Y. Zhu, A. Torralba, W. Matusik, *Nature* **2019**, *569*, 698.
[2] C. M. Boutry, M. Negre, M. Jorda, O. Vardoulis, A. Chortos, O. Khatib, Z. Bao, *Sci. Robot.* **2018**, *3*, aau6914.
[3] Q. Hua, J. Sun, H. Liu, R. Bao, R. Yu, J. Zhai, C. Pan, Z. L. Wang, *Nat. Commun.* **2018**, *9*, 244.
[4] M. Cai, Z. Jiao, S. Nie, C. Wang, J. Zou, J. Song, *Sci. Adv.* **2021**, *7*, abl8313.
[5] N. Bai, L. Wang, Y. Xue, Y. Wang, X. Hou, G. Li, Y. Zhang, M. Cai, L. Zhao, F. Guan, X. Wei, C. F. Guo, *ACS Nano* **2022**, *16*, 4338.
[6] Y. Tagawa, S. H. Lee, T. Someya, T. Yokota, *Adv. Electron. Mater.* **2023**, *9*, 2201304.
[7] R. Liu, B. Ji, M. Lei, F. Hu, J. Luo, B. Zhou, *Appl. Mater. Today* **2025**, *42*, 102614.
[8] J. Park, Y. Lee, S. Cho, A. Choe, J. Yeom, Y. G. Ro, J. Kim, D.-H. Kang, S. Lee, H. Ko, *Chem. Rev.* **2024**, *124*, 1464.
[9] J.-H. Zhang, Z. Li, J. Xu, J. Li, K. Yan, W. Cheng, M. Xin, T. Zhu, J. Du, S. Chen, X. An, Z. Zhou, L. Cheng, S. Ying, J. Zhang, X. Gao, Q. Zhang, X. Jia, Y. Shi, L. Pan, *Nat. Commun.* **2022**, *13*, 5839.
[10] R. Yang, A. Dutta, B. Li, N. Tiwari, W. Zhang, Z. Niu, Y. Gao, D. Erdely, X. Xin, T. Li, H. Cheng, *Nat. Commun.* **2023**, *14*, 2907.
[11] Z. Li, S. Zhang, Y. Chen, H. Ling, L. Zhao, G. Luo, X. Wang, M. C. Hartel, H. Liu, Y. Xue, R. Haghniaz, K. Lee, W. Sun, H. Kim, J. Lee, Y. Zhao, Y. Zhao, S. Emaminejad, S. Ahadian, N. Ashammakhi, M. R. Dokmeci, Z. Jiang, A. Khademhosseini, *Adv. Funct. Mater.* **2020**, *30*, 2003601.
[12] S. Wang, F. Gao, Y. Hu, S. Zhang, H. Shang, C. Ge, B. Tan, X. Zhang, J. Zhang, P. Hu, *Chem. Eng. J.* **2022**, *443*, 136446.
[13] Y. Zhang, J. Yang, X. Hou, G. Li, L. Wang, N. Bai, M. Cai, L. Zhao, Y. Wang, J. Zhang, K. Chen, X. Wu, C. Yang, Y. Dai, Z. Zhang, C. F. Guo, *Nat. Commun.* **2022**, *13*, 1317.
[14] N. Bai, L. Wang, Q. Wang, J. Deng, Y. Wang, P. Lu, J. Huang, G. Li, Y. Zhang, J. Yang, K. Xie, X. Zhao, C. F. Guo, *Nat. Commun.* **2020**, *11*, 209.
[15] J. Yang, Z. Li, Y. Wu, Y. Shen, M. Zhang, B. Chen, G. Yuan, S. Xiao, J. Feng, X. Zhang, Y. Tang, S. Ding, X. Chen, T. Wang, *Sci. Bull.* **2024**, *69*, 2221.
[16] H. Tian, Y. Jiang, Y. Song, T. Wang, J. Xue, F. Zhang, Y. Liu, Z. Xue, K. Wang, Y. Zhao, *ACS Sens.* **2025**, *10*, 2030.
[17] X. W. Zhu, Y. N. Zhao, Z. Y. Zhou, et al., *J. Colloid Interface Sci.* **2025**, *699*, 138291.
[18] L. Wu, X. Li, J. Choi, Z.-J. Zhao, L. Qian, B. Yu, I. Park, *Adv. Funct. Mater.* **2024**, *34*, 2312370.
[19] X. Chen, Y. Luo, Y. Chen, S. Li, S. Deng, B. Wang, Q. Zhang, X. Li, X. Li, C. Wang, J. He, H. Tian, J. Shao, *Adv. Sci.* **2024**, *11*, 2408082.
[20] L. Song, Z. Wang, S. Chen, Y. Shen, J. Yin, R. Wang, *Adv. Mater.* **2025**, *37*, 2417978.
[21] W. Z. Zhu, J. Wang, W. Sun, S. Zhou, M. He, *Chem. Eng. J.* **2023**, *451*, 138335.
[22] H. Liu, H. Chu, H. Yuan, D. Li, W. Deng, Z. Fu, R. Liu, Y. Liu, Y. Han, Y. Wang, Y. Zhao, X. Cui, Y. Tian, *Nano-Micro Lett.* **2024**, *16*, 69.
[23] S. P. Li, T. S. Yin, Z. J. Huang, *ACS Mater. Lett.* **2024**, *6*, 1686.
[24] Z. W. Lin, S. S. Duan, M. Y. Liu, et al., *Adv. Mater.* **2024**, *36*, 2306880.
[25] H. Liu, R. Liu, K. Chen, Y. Liu, Y. Zhao, X. Cui, Y. Tian, *Chem. Eng. J.* **2023**, *461*, 141966.
[26] Q. Ge, Z. Chen, J. Cheng, B. Zhang, Y.-F. Zhang, H. Li, X. He, C. Yuan, J. Liu, S. Magdassi, S. Qu, *Sci. Adv.* **2021**, *7*, aba4261.
[27] J. Idaszek, M. Costantini, T. A. Karlsen, J. Jaroszewicz, C. Colosi, S. Testa, E. Fornetti, S. Bernardini, M. Seta, K. Kasarello, R. Wrzesien, S. Cannata, A. Barbetta, C. Gargioli, J. E. Brinchman, W. Swieszkowski, *Biofabrication* **2019**, *11*, 044101.
[28] W. Zhang, C. Zeng, M. Zhang, C. Zhao, D. Chao, G. Zhou, C. Zhang, *Angew. Chem., Int. Ed.* **2025**, *64*, 202413728.
[29] J. Meng, J. Luo, H. Wang, Y. Quan, J. Li, X. Sun, *Chem. Commun.* **2022**, *58*, 6821.
[30] Z. Hui, Y. Wang, Z. Zhang, R. Zhang, J. Zhou, W. Hou, L. Yin, H. Dai, Z. Xia, T. Zhang, W. Huang, G. Sun, *Adv. Mater.* **2025**, 10285.
[31] S. M. Taromsari, M. Salari, H. H. Shi, et al., *Adv. Mater.* **2025**, *37*, 2406349.

[32] S. A. Jaseem, P. Rahmani, T. Sakorikar, J. Ma, O. Almutairi, M. A. Voinov, A. I. Smirnov, B. Chen, M. D. Dickey, *Adv. Funct. Mater.* **2025**.

[33] G. Ge, Y.-Z. Zhang, W. Zhang, W. Yuan, J. K. El-Demellawi, P. Zhang, E. Di Fabrizio, X. Dong, H. N. Alshareef, *ACS Nano* **2021**, *15*, 2698.

[34] Y. Zhu, J. Liu, T. Guo, J. J. Wang, X. Tang, V. Nicolosi, *ACS Nano* **2021**, *15*, 1465.

[35] T. Shui, M. Pan, A. Li, H. Fan, J. Wu, Q. Liu, H. Zeng, *Chem. Mater.* **2022**, *34*, 8613.

[36] Y. Zhang, L. X. Liu, S. X. Yin, et al., *Adv. Funct. Mater.* **2025**.

[37] J. Lai, T. Xiong, S. Chen, Z. Zhou, J. Liu, B. Yang, R. S. Tuan, Z. A. Li, *Adv. Sci.* **2025**, *12*, 09449.

[38] Y. Ao, L. Jin, S. Wang, B. Lan, G. Tian, T. Xu, L. Huang, Z. Wang, Y. Sun, T. Yang, W. Deng, F. Yang, W. Yang, *Nano-Micro Lett.* **2025**, *17*, 320.

[39] J. Park, J. Kim, J. Hong, H. Lee, Y. Lee, S. Cho, S.-W. Kim, J. J. Kim, S. Y. Kim, H. Ko, *NPG Asia Mater* **2018**, *10*, 163.

[40] A. Pragya, T. K. Ghosh, *Adv. Mater.* **2023**, *35*, 2300912.

[41] Z. Q. Liu, M. A. Meyers, Z. F. Zhang, R. O. Ritchie, *Prog. Mater Sci.* **2017**, *88*, 467.

[42] H. Dai, W. Dai, Z. Hu, W. Zhang, G. Zhang, R. Guo, *Adv. Sci.* **2023**, *10*, 2207192.

[43] Y. Li, N. N. Bai, Y. Chang, et al., *Chem. Soc. Rev.* **2025**, *54*, 4651.

[44] G. Libo, M. Wang, W. D. Wang, et al., *Nano-Micro Lett.* **2021**, *13*, 140.

[45] J. Xu, H. Li, Y. Yin, et al., *npj Flex. Electron.* **2022**, *6*, 62.

[46] R. Chen, T. Luo, J. Wang, R. Wang, C. Zhang, Y. Xie, L. Qin, H. Yao, W. Zhou, *Nat. Commun.* **2023**, *14*, 6641.

[47] Y. Zhao, N. Yang, X. Chu, F. Sun, M. U. Ali, Y. Zhang, B. Yang, Y. Cai, M. Liu, N. Gasparini, J. Zheng, C. Zhang, C. Guo, H. Meng, *Adv. Mater.* **2023**, *35*, 2211617.

[48] Y. F. He, Y. Cheng, C. H. Yang, C. F. Guo, *Nat. Mater.* **2024**, *23*, 1107.

[49] J. L. Shi, S. Xie, Z. G. Liu, M. K. Cai, C. F. Guo, *Natl. Sci. Rev.* **2024**, *11*, nwae351.

[50] Y. Li, W. Zhang, C. Zhao, W. Li, E. Dong, M. Xu, H. Huang, Y. Yang, L. Li, L. Zheng, M. Mao, S. Yao, L. Wang, J. Ma, X. Wang, W. Huang, *Adv. Mater.* **2024**, *36*, 2405405.

[51] J. Baek, Y. Zhang, F. Qin, X. Fu, M.-S. Kim, H.-W. Song, J.-H. Oh, G. Kim, S. Lee, *Adv. Funct. Mater.* **2025**, *35*, 2414050.